CrossMark

ORIGINAL PAPER

Poypyrrole/molybdenum trioxide/graphene nanoribbon ternary nanocomposite with enhanced capacitive performance as an electrode for supercapacitor

Feng-Hao Hsu[1] · Tzong-Ming Wu[1]

Abstract A polypyrrole/molybdenum trioxide/graphene nanoribbon (PPy/MoO$_3$/GNR) ternary nanocomposite was successfully synthesized via an in situ method. Fourier transform infrared spectroscopy and X-ray photoelectron spectroscopy analyses show that MoO$_3$ was successfully combined with the GNRs. The one-dimensional morphology was observed using field emission scanning electron microscopy and transmission electron microscopy. The electrochemical tests show that the PPy/MoO$_3$/GNR ternary nanocomposite exhibits the highest specific capacitance (844 F g^{-1}) among the investigated materials and exhibits good cycling stability for 1000 cycles. These results collectively demonstrate that the combination of each component can efficiently increase the specific capacitance and cycling stability. As such, the method reported herein represents a promising approach for fabricating supercapacitor electrode materials.

Keywords Polypyrrole · Graphene nanoribbon · Molybdenum trioxide · Ternary nanocomposite · Supercapacitor

Introduction

In recent years, worldwide energy shortages have spurred many scientists and researchers to investigate alternative energy sources or to develop high-performance energy storage systems. Energy storage systems, such as electrochemical capacitors, also known as supercapacitors, have attracted extensive attention over the past few decades owing to their high power and energy densities and good long-term cycling stability [1, 2]. In general, according to the energy storage mechanism, supercapacitors can be classified into electrical double-layer capacitors (EDLCs) and pseudocapacitors. The energy storage principle of EDLCs is based on the accumulation of charge at the electrode/electrolyte interface, where high specific-surface-area materials such as carbon-based compounds are commonly used as electrode materials [3]. Among the carbon materials investigated in EDLCs, graphene-based materials have attracted much attention because of their excellent electrical conductivity [4], specific surface area [5], and good mechanical properties [6]. In particular, a new morphology of graphene called graphene nanoribbon (GNR) is a strip of graphene with a high length-to-width ratio; GNR has attracted significant attention over the past few years. Because of its unique physical properties, GNR is used in numerous electronic devices, including transistors, sensors, and solar cells [7–9]. In addition, due to its particular structure and high specific surface area, GNR has also been investigated as an electrode material in supercapacitors [10, 11].

Charge storage in a pseudocapacitor is attributed to fast faradaic reactions between the electrode and electrolyte, where electrochemically active materials, such as metal oxides and intrinsic conducting polymers, are commonly used as electrodes. Among metal oxides, ruthenium oxide (RuO$_2$) is the most widely investigated material in supercapacitor applications due to its high specific capacitance; however, its high cost hinders its broad application in energy storage devices [12]. Therefore, various metal oxides such as MnO$_2$, V$_2$O$_5$, and Fe$_2$O$_3$ have attracted attention because of their low cost and high natural abundance [13–15]. Molybdenum trioxide (MoO$_3$) has potential applications in supercapacitors owing to its particular nanostructure [16, 17], high electrochemical

✉ Tzong-Ming Wu
tmwu@dragon.nchu.edu.tw

[1] Department of Materials Science and Engineering, National Chung Hsing University, 250 Kuo Kuang Road, Taichung 402, Taiwan

activity, environmental compatibility, and low cost [18]. In particular, several investigations have indicated that MoO_3 exhibits a capacitance equivalent to that of RuO_2 at low loading amounts in composites [19, 20]. Therefore, an investigation of the performance of MoO_3 in a supercapacitor would be interesting. Polypyrrole (PPy) is an intrinsic conducting polymer that offers many attractive properties, including high conductivity, good chemical stability, easy synthesis, low toxicity, and low cost; it has, therefore, been extensively investigated for use in supercapacitors [21, 22]. However, irrespective of whether supercapacitors are fabricated using metal oxides or intrinsic conducting polymers, the poor cycling stability remains the most critical problem limiting their further development.

Many researchers have suggested that the combination of an EDLC and a pseudocapacitor is a viable and efficient approach for improving the cycling stability of pseudocapacitors. Recently, Xu et al. synthesized a hierarchical PPy/graphene nanocomposite as a graphene-based, two-component nanocomposite via in situ polymerization; their fabricated nanocomposite exhibited an excellent electrochemical capacitance of 318.6 F g^{-1} and good cycling stability [23]. Liu et al. synthesized a graphene/PPy intercalating nanocomposite that exhibited a high specific capacitance of 650 F g^{-1} and retained a high specific capacitance after 5000 cycles [24]. Additionally, some ternary nanocomposites comprising a metal oxide, a conducting polymer, and a carbon material have also been investigated as supercapacitor electrodes. For example, Wang et al. prepared a graphene/SnO_2/PPy ternary composite that exhibits a high specific capacitance of 616 F g^{-1} that only decays 2 % after 1000 cycles [25]. Similarly, Han et al. prepared a sandwich-structured MnO_2/PPy/graphene hybrid composite with a specific capacitance of 404 F g^{-1} that retained a high specific capacitance after 5000 cycles [26]. However, the literature contains no reports of investigations of GNR-based ternary nanocomposites in supercapacitors.

Herein, we report the synthesis of a new ternary nanocomposite, which comprises PPy, MoO_3, and GNR, as an electrode material for supercapacitors; we, thus, expect this material to exhibit improved specific capacitance and cycling stability. The morphology, electrochemical properties, and electric capacity of the prepared composite are described in detail.

Experimental

Preparation of GNR

GNR was prepared using the chemical oxidation method in the presence of strong oxidation agent and strong acid. A mass of 0.05 g multi-wall carbon nanotubes (MWCNTs) was mixed in 10 mL H_2SO_4 (98 %, Aldrich Chemical Co.) and stirred for 1 h at room temperature. $KMnO_4$ powders (0.25 g) were

added into the above-mentioned mixture and reacted for 1 h at room temperature. Then, the solution was kept at a high temperature of 80 °C and reacted for 1 h. After reaction, the solution was added into 5 % H_2O_2 solution and stood for 24 h. The products were then filtered and washed several times with DI-water until the solution became acid-free. Finally, the products were dried under vacuum at 60 °C for 24 h.

In situ synthesis of PPy/GNR nanocomposite

The PPy/GNR nanocomposite was synthesized via in situ chemical oxidative polymerization. In a typical synthesis experiment, GNR powders (16 mg) were added into 40 mL 1 M HCl solution in a reaction vessel and sonicated for 1 h. Pyrrole monomer (0.08 mL; 98 %, Aldrich Chemical Co.) was added into the GNR dispersed solution and stirred for 30 min. Then, ammonium persulfate (APS) solution (13 mg APS was dissolved in 10 mL 1 M HCl solution) was slowly dropped into the pyrrole monomer/GNR mixed solution and reacted for 3 h at 0 °C. After 3 h reaction, the PPy/GNR nanocomposite products were poured into large amount of methanol to terminate the polymerization. Finally, the products were filtered and washed several times with DI water and methanol. It was then dried under vacuum at 60 °C for 24 h.

In situ synthesis of PPy/MoO$_3$/GNR ternary nanocomposite

First, in the preparation of MoO_3/GNR composite, GNR powders (20 mg) were immersed in 15 mL DI water and sonicated for 1 h. The metal oxide precursor $MoCl_5$ (99.6 %, Alfa Aesar) 0.137 g was dissolved in 2 mL DI water, and citric acid solution (citric acid 10 mg was dissolved in 1 mL DI-water) was simultaneously prepared. Then, these solutions were simultaneously added into GNR dispersion solution and stirred for 30 min. Finally, the solution was poured into a Teflon stainless steel autoclave and kept in an oven at 160 °C hydrothermal for 1 h. When the autoclave was left to cool to room temperature, the dark-green solution was filtered and washed with DI water. The products were then dried under vacuum at 60 °C for 24 h.

Second, the PPy/MoO_3/GNR ternary nanocomposite was also synthesized via in situ chemical oxidative polymerization. MoO_3/GNR composite powders (16 mg) were immersed in 40 mL 1 M HCl solution in a reaction vessel and sonicated for 1 h. Then, 0.08 mL pyrrole monomer was added into MoO_3/GNR dispersion solution and stirred for 30 min. After being stirred for 30 min, APS solution (13 mg APS was dissolved in 10 mL 1 M HCl solution) was slowly dropped into the pyrrole monomer/MoO_3/GNR solution and then reacted at 0 °C for 3 h. After 3 h reaction, the PPy/MoO_3/GNR ternary nanocomposite products were added into large amount of methanol to stop reaction. Finally, the product was filtered

and washed with DI water and methanol for several times and then dried under vacuum at 60 °C for 24 h.

Material characterization

Fourier transform infrared (FTIR) spectra were recorded on a PerkinElmer Spectrum One spectrometer with the resolution of 4 cm^{-1}. The FTIR samples were pressed into tablets with potassium bromide (KBr). The X-ray photoelectron spectroscopy (XPS) analysis was carried out on a ULVAC-PHI, PHI 5000 VersaProbe/Scanning ESCA spectrometer. The morphology was observed by field emission scanning electron microscope (FESEM) and transmission electron microscopy (TEM). FESEM measurements were conducted at 3 kV using a JEOL JSM-6700F field emission instrument. The samples for TEM measurement were prepared by casting a drop of the sample suspended in ethanol on a copper grid covered with carbon. The specific surface area and porosity of the nanocomposites were measured from nitrogen absorption-desorption on the Micromeritics ASAP 2010 Brunauer-Emmett-Teller (BET) instrument.

Electrochemical measurements

The electrochemical measurements were carried in a three-electrode cell system using CHI 6271D electrochemical analysis instrument. According to previous investigations, the addition of Nafion in the working electrode contains high ion conductivity and exhibits proton conductivity because of the presence of sulfonate groups in the polymer chain, thus improving the ion transport performance [27, 28]. Therefore, the working electrode was prepared according to the following steps. Samples (1 mg) were dispersed in 2-mL ethanol solution containing 0.01 mL Nafion solution as a binder and then sonication for 1 h. Then, 0.02 ml suspended solution was dropped onto the glassy carbon electrode and dried before electrochemical analysis. The potential range of cyclic voltammongram (CV) testing was measured from −0.2 to 0.8 V (vs. Ag/AgCl) and using 1 M H$_2$SO$_4$ solution as an electrolyte. Galvanostatic charge/discharge curves were measured in the potential range of −0.2 to 0.8 V at a current density of 5 A g^{-1}. The electrochemical impedance spectroscope (EIS) test was analyzed in a range from 10^5 to 1 Hz of frequency with alternate current amplitude of 5 mV.

The specific capacitance (C_{sp}) of all of samples was obtained from CV curves by using the following equation [29]:

$$C_{sp} = \int I \mathrm{d}V \Big/ 2m\nu V \qquad (1)$$

where C_{sp} is the specific capacitance (F g^{-1}), ν is the potential scan rate (mV s^{-1}), m is the mass of electro-active material on the glassy carbon electrode, $\int I \, \mathrm{d}V$ term is the area of CV curve, and V is the scan potential range.

The gravimetric specific capacitance was obtained from the following equation [24]:

$$C_{sp} = I \, \Delta t \Big/ m \, \Delta V \qquad (2)$$

where I is the discharge current (A), Δt is the discharge time (s), ΔV is the potential range during the discharge process (V), and m is the mass of electro-active material (g).

Results and discussions

The FTIR spectra used to identify the components of all the samples are shown in Fig. 1. The GNR absorption peak at 1720 cm^{-1} is due to the C=O stretching vibration; its appearance in the spectrum suggests the existence of oxygen-containing functional groups on the GNR surface after the chemical oxidation process. In the case of pure PPy, the peaks at 1550 and 1455 cm^{-1} are attributed to the C–C and C–N stretching vibrations in the pyrrole ring. Other absorption peaks at 1045 and 905 cm^{-1} are assigned to C–H deformation and C–H out-of-plane vibrations, respectively. Three significant peaks are observed at 995, 863, and 554 cm^{-1} in the spectrum of pure MoO$_3$; these peaks are assigned to Mo=O, Mo–O, and Mo–O–Mo, respectively [30]. The spectrum of the MoO$_3$/GNR composite exhibits three weak absorption peaks attributable to MoO$_3$, thereby confirming the presence of MoO$_3$ in the GNR matrix. The absorption peaks in the spectra of PPy/GNR and the PPy/MoO$_3$/GNR ternary nanocomposite (curves e and f in Fig. 1) are similar to those in the spectrum of pure PPy. Moreover, the absorption peaks of PPy at 1550 and 905 cm^{-1} are slightly shifted to approximately 1535 and 885 cm^{-1} in the spectrum of each nanocomposite. This result is attributed to the interaction between PPy and GNR or to that between PPy and MoO$_3$/GNR. Furthermore, the three main absorption peaks of MoO$_3$ are not observed in
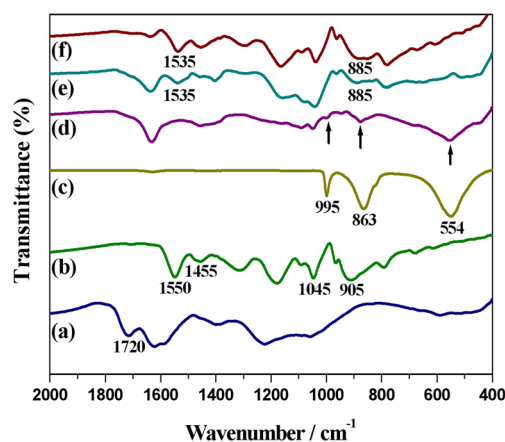
Fig. 1 The FTIR spectrum of **a** GNR, **b** pure PPy, **c** pure MoO$_3$, **d** MoO$_3$/GNR composite, **e** PPy/GNR nanocomposite, and **f** PPy/MoO$_3$/GNR ternary nanocomposite
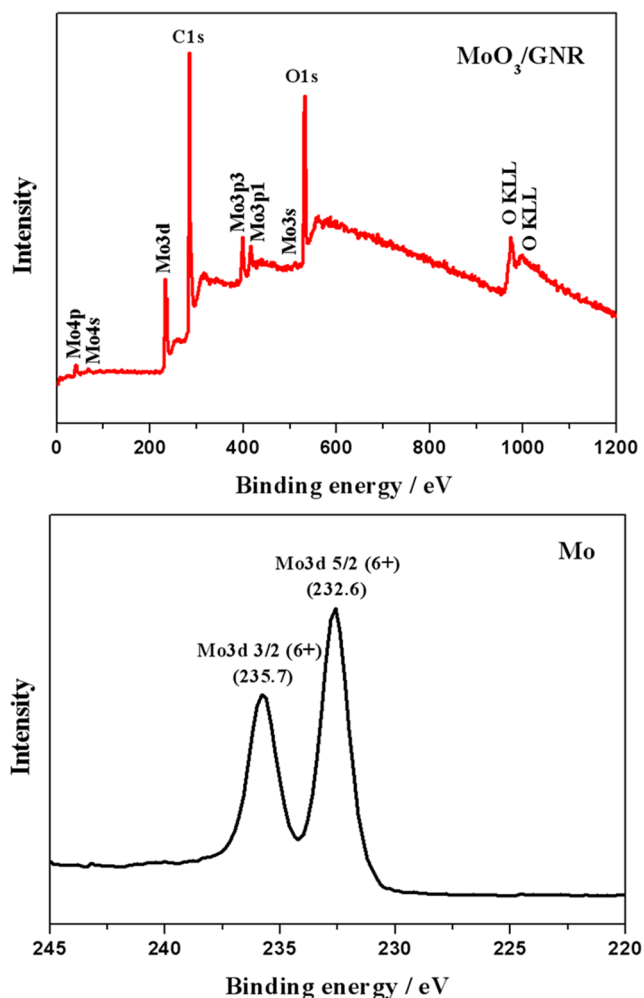
Fig. 2 The XPS spectrum of MoO₃/GNR composite and the Mo 3d of MoO₃/GNR

the spectrum of the PPy/MoO₃/GNR ternary nanocomposite due to the PPy coating on the MoO₃/GNR surface.

To further demonstrate that MoO₃ was successfully synthesized in the composite, we used XPS analysis to analyze the chemical composition of the MoO₃/GNR composites. Figure 2 shows the full spectra of the MoO₃/GNR composite and the Mo 3d binding energy region. In the full spectrum of the MoO₃/GNR composite, peaks of Mo and O are clearly observed, suggesting the presence of MoO₃ in the composite. The spectral lines of the Mo 3d binding energy reveal the two characteristic peaks of MoO₃: Mo $3d_{5/2}$ 6+ at 232.6 eV and Mo $3d_{3/2}$ 6+ at 235.7 eV. This result confirms the existence of MoO₃ in the composite [31]. Moreover, the MoO₃ content of the composite was quantitatively determined from the XPS peak profile, which revealed that the MoO₃ content in the composite was only 4.6 %.

The TEM images of pristine MWCNTs and GNRs are shown in Fig. 3a, 3b, respectively. The diameters of the MWCNTs are approximately 50 nm, and they exhibit a smooth edge. After chemical modification, the tube-like

structure of the MWCNTs is completely unzipped because the oxidant attacks the MWCNT axial structure to form GNRs; therefore, the diameter of the GNRs apparently increased from 50 to about 100 nm, and the edges become distorted. The FESEM and TEM images of pure PPy in Fig. 3c show nanoparticle aggregates with a diameter of approximately 150 nm. The images of the PPy/GNR nanocomposite are shown in Fig. 3d. The one-dimensional morphology with a diameter about 120 nm can be observed, and the PPy nanoparticle is also evidently reduced when in the presence of GNR. This increased diameter of the GNRs and reduced size of PPy nanoparticle are attributed to the coated PPy on the GNR surface. In the case of Fig. 3e, the images of PPy/MoO₃/GNR ternary nanocomposite also clearly show the one-dimensional morphology with about 120 nm, demonstrating that the PPy also coated on the MoO₃/GNR composite surface. These results might be attributable to the strong interaction between PPy and the GNRs or the MoO₃/GNRs. Moreover, the BET surface geometric area of the PPy/GNR and PPy/MoO₃/GNR nanocomposites analyzed by using nitrogen absorption experiment is correspondingly 73.52 and 76.13 m² g⁻¹. The porosity of the two types of nanocomposite also measured by using the same method is 0.27 and 0.29 cm³ g⁻¹, respectively.

The electrochemical properties of the pure materials and synthesized nanocomposites were analyzed by CV test using a three-electrode system. Figure 4 shows the CV curves of pure materials and nanocomposites at a scan rate 5 mV s⁻¹. Compared with pure PPy, the CV curve of GNR is slightly close to a rectangular shape, demonstrating that the GNR possess EDLC behavior [32]. The current response and area of the CV curve represent the electrochemical performance and the specific capacitance of the electrode material, respectively. The current response and area of the CV curves for all nanocomposites are greater than those for PPy and GNRs. Thus, the PPy/GNR and PPy/MoO₃/GNR nanocomposites exhibit excellent electrochemical performance and high specific capacitance. The highest specific capacitance calculated using Eq. 1 is 844 F g⁻¹ for the PPy/MoO₃/GNR ternary nanocomposite; this specific capacitance is substantially greater than that of pure PPy (243 F g⁻¹), indicating the synergistic effect of each component. The specific capacitance of the PPy/MoO₃/GNR ternary nanocomposite is also slightly higher than that of the PPy/GNR two-component nanocomposite, indicating that the combination of GNR with two types of pseudocapacitor (i.e., PPy and MoO₃) might more effectively increase the specific capacitance via the synergistic effect of each component.

Figure 5 shows the CV curves of PPy/MoO₃/GNR ternary nanocomposites with various scan rates. The CV curves of nanocomposites reveal the rectangular shape and do not significantly change when the scan rate increased. These results show that the nanocomposites possess ideal capacitive

Fig. 3 TEM images of **a** MWCNT and **b** GNR. FESEM images of **c** pure PPy, **d** PPy/GNR nanocomposite, and **e** PPy/MoO$_3$/ GNR ternary nanocomposite. (Inset the TEM images of **c** pure PPy, **d** PPy/GNR nanocomposite, and **e** PPy/MoO$_3$/GNR ternary nanocomposite are also shown in this figure)
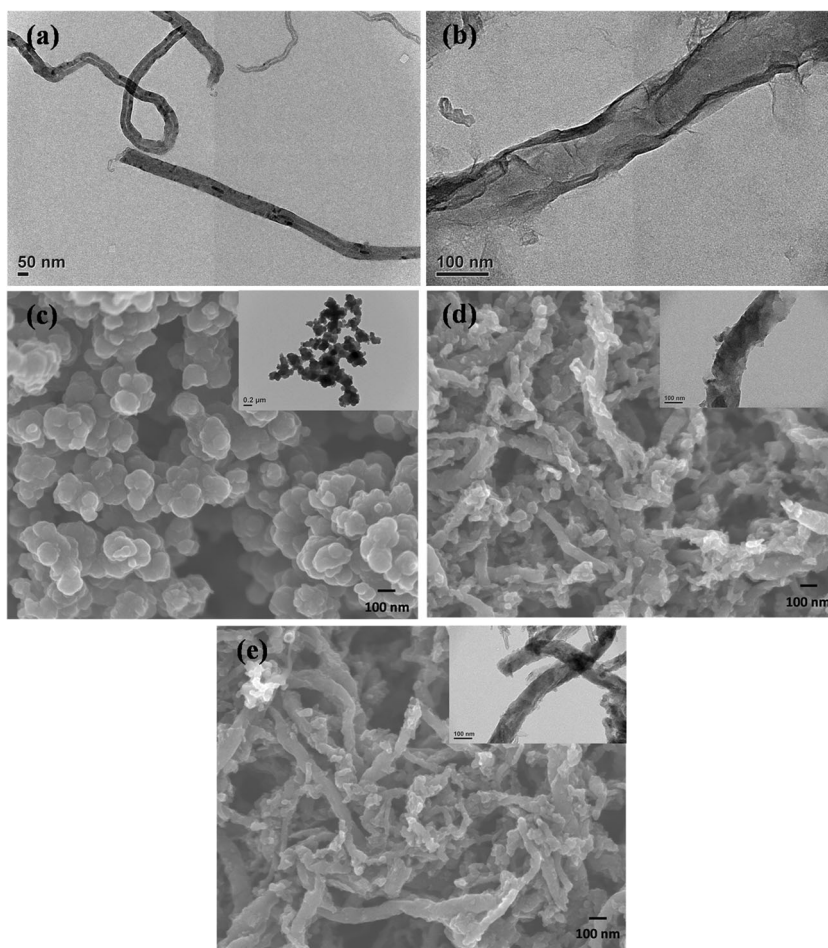

behavior and good rate capability. Figure 6 shows the specific capacitance trends for all of the samples as the scan rate was increased from 5 to 200 mV s^{-1}. These scan rate tests reveal the rate capability and the transport performance of the ions in the materials. For all of the samples, the specific capacitance decreases with increasing scan rate. Notably, the specific capacitance of the PPy/MoO$_3$/GNR ternary nanocomposite

remains as high as 504 F g^{-1} at a high scan rate, demonstrating that the PPy/MoO$_3$/GNR ternary nanocomposite exhibits better rate capability and ion transportation performance than the other investigated samples. The decay of the specific
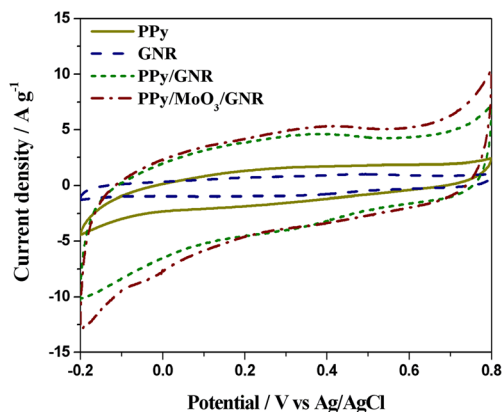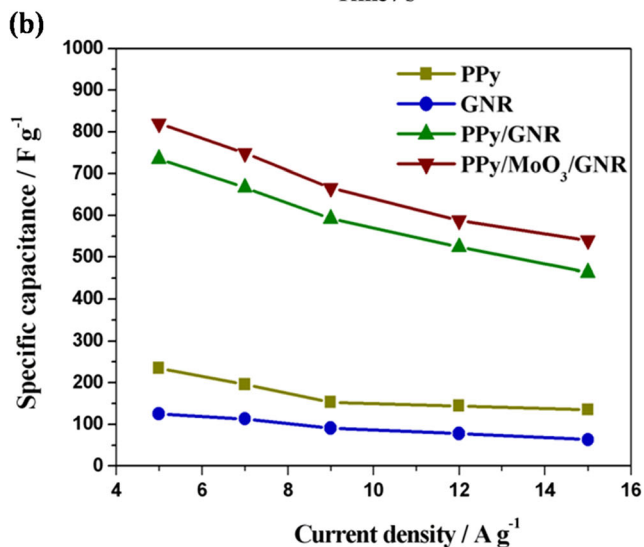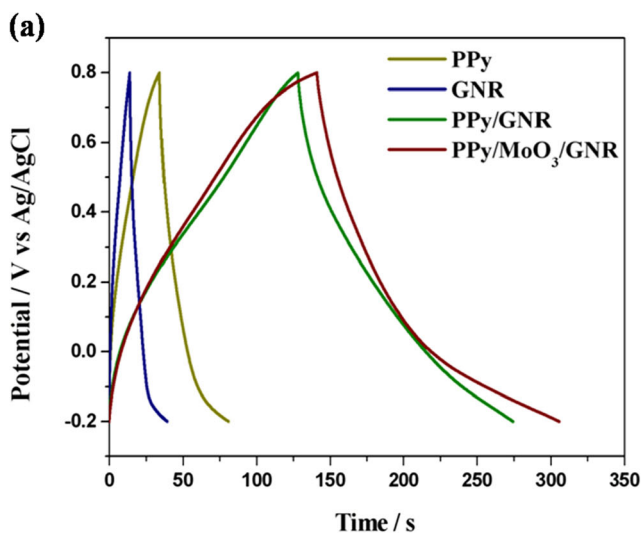

Fig. 4 CV curves of pure PPy, GNR, and PPy/GNR nanocomposite and PPy/MoO$_3$/GNR ternary nanocomposite
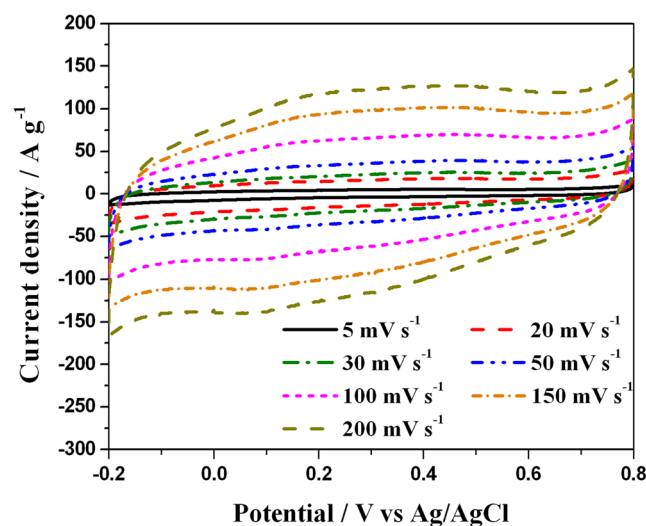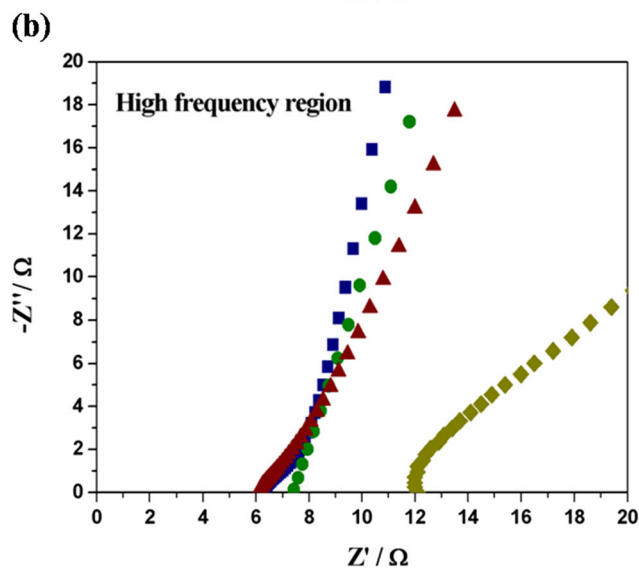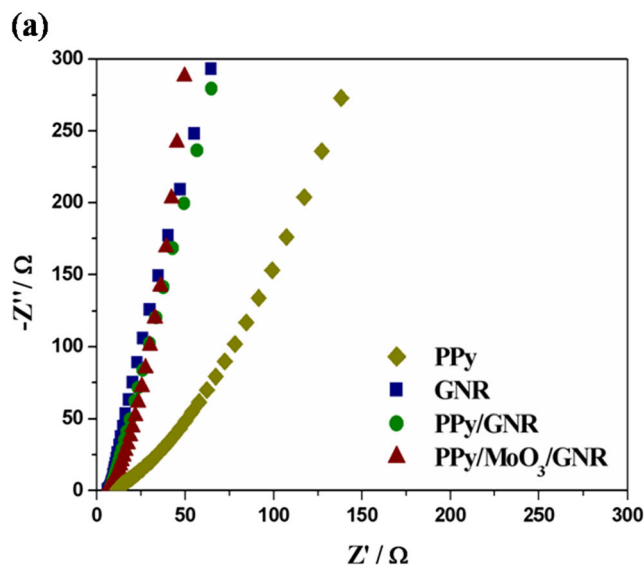

Fig. 5 CV curves of PPy/MoO$_3$/GNR ternary nanocomposite with various scan rates
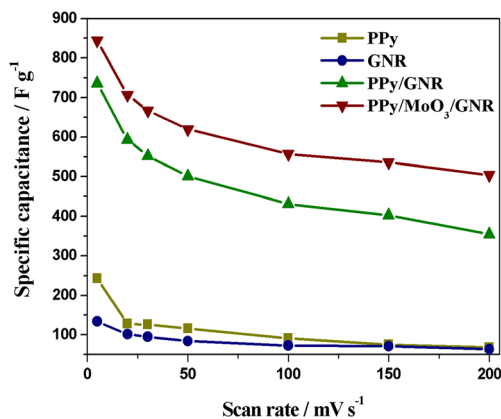
Fig. 6 Specific capacitance values of pure PPy, GNR, and PPy/GNR nanocomposite and PPy/MoO$_3$/GNR ternary nanocomposite at various scan rates in the range of 5 to 200 mV s^{-1}
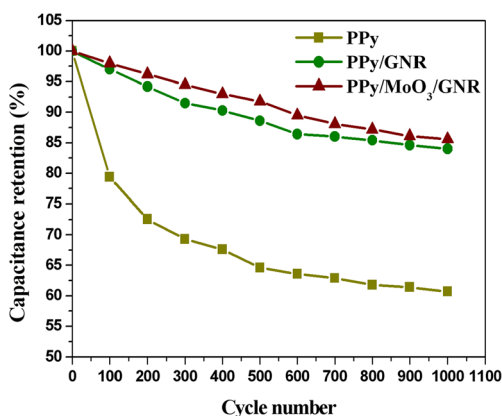

Fig. 7 **a** Galvanostatic charge/discharge curve of pure PPy, GNR, and PPy/GNR nanocomposite and PPy/MoO$_3$/GNR ternary nanocomposite at a current density of 5 A g^{-1}. **b** Specific capacitance values of pure PPy, GNR, and PPy/GNR nanocomposite and PPy/MoO$_3$/GNR ternary nanocomposite at various current densities in the range of 5 to 15 A g^{-1}

Fig. 8 Nyquist plots from EIS test of pure PPy, GNR, and PPy/GNR nanocomposite and PPy/MoO$_3$/GNR ternary nanocomposite at **a** overall region and **b** high-frequency region in 1 M H$_2$SO$_4$ solution

capacitance is attributed to the charge not being able to completely accumulate in the materials at high scan rates [25].

Galvanostatic charge/discharge tests, which were performed in the potential range from −0.2 to 0.8 V at a current density of 5 A g^{-1}, were also used to characterize the electrochemical performance and specific capacitance properties of the electrodes. As evident from Fig. 7a, the nanocomposites of PPy/GNR and PPy/MoO$_3$/GNR exhibit longer charge/discharge times compared to pure PPy and GNR. This result also indicates that the combination of an EDLC and a pseudocapacitor can increase the electrochemical performance and specific capacitance through a synergistic effect. Furthermore, the highest specific capacitance calculated using Eq. 2 was 825 F g^{-1} for the PPy/MoO$_3$/GNR ternary nanocomposite at a current density 5 A g^{-1}; the calculated specific

Fig. 9 Cycle stability of pure PPy and PPy/GNR nanocomposite and PPy/MoO$_3$/GNR ternary nanocomposite at a current density 15 A g^{-1}

capacitances of all of the samples matched those calculated on the basis of the CV results. Figure 7b shows the trends of specific capacitance as the current density was increased from 5 to 15 A g^{-1}. The decay trends of specific capacitance are also consistent with the results of the CV tests, which indicate that the PPy/MoO$_3$/GNR ternary nanocomposite exhibits the best rate capability and ion transportation performance among the investigated materials.

Electrochemical impedance spectroscopy is a commonly used technique to analyze the electrochemical performance of electrode materials. Typical Nyquist plots for all the investigated samples are shown in Fig. 8. Each Nyquist plot exhibits two distinct regions: a high-frequency region and a low-frequency region. The intercepts of the real axes, which are related to the solution resistance (R_s) values for the pure PPy, GNR, PPy/GNR, and PPy/MoO$_3$/GNR, are 12.1, 6.25, 7.29, and 6.08 Ω, respectively [33]. The high-frequency regions of the Nyquist plots for GNR, PPy/GNR, and PPy/MoO$_3$/GNR show an inconspicuous semicircle, indicating a lower charge transfer resistance for these samples. The sloped segment in the low-frequency region represents the ion diffusion resistance of the electrode material [34]. The results clearly indicate that the GNR and nanocomposites exhibit larger slopes than pure PPy. This result demonstrates that the GNR and nanocomposites exhibit lower ion diffusion resistances.

The cycling stability is an important index for a supercapacitor. Herein, we evaluated the cycling stability by repeating charge/discharge tests at a current density 15 A g^{-1} in the potential range from −0.2 to 0.8 V for 1000 cycles, as shown in Fig. 9. The calculated specific capacitance retention percentages for pure PPy, the PPy/GNR nanocomposite, and the PPy/MoO$_3$/GNR ternary nanocomposite after 1000 cycles are 60.7, 84, and 85.6 %, respectively. These results clearly indicate that the PPy/MoO$_3$/GNR ternary nanocomposite exhibits long-term cycling stability, which might be attributable to the good interaction between the GNR EDLC and the MoO$_3$ and PPy pseudocapacitors.

Conclusions

The PPy/MoO$_3$/GNR ternary nanocomposite was successfully synthesized by in situ method with a high specific capacitance of 844 F g^{-1} and long cycle stability. The FTIR and XPS spectra show that the MoO$_3$ indeed exists on the GNR surface. The electrochemical measurements revealed an excellent capacitive behavior and rate capability for the PPy/MoO$_3$/GNR ternary nanocomposite, indicating that the combination of EDLC and pseudocapacitor could efficiently increase specific capacitance and cycle stability by synergistic effect. The EIS measurement shows that the nanocomposites also possess lower resistance of charge transfer and lower ion diffusion resistance, thus improving the ion transfer efficient of nanocomposite. These results could provide an approach and technology to develop the high-performance materials in the field of supercapacitor.

References

1. Lu XJ, Zhang F, Dou H, Yuan CZ, Yang SD, Hao L, Shen LF, Zhang LJ, Zhang XG (2012) Electrochim Acta 69:160–166
2. Liu C, Li F, Ma LP, Cheng HM (2010) Adv Mater 22:E28–E62
3. Qu DY, Shi H (1998) J Power Sources 74:99–107
4. Bolotin KI, Sikes KJ, Jiang Z, Klima M, Fudenberg G, Hone J, Kim P, Stormer HL (2008) Solid State Commun 146:351–355
5. Stoller Meryl D, Park SJ, Zhu YW, An JH, Ruoff Rodney S (2008) Nano Lett 8:3498–3502
6. Lee CG, Wei XD, Kysar Jeffrey W, Hone J (2008) Science 321:385
7. de Oliveira HP, Sydlik Stefanie A, Swager Timothy M (2013) J Phy Chem C 117:10270–10276
8. Konwer S, Boruah R, Dolui Swapan K (2011) J Elctron Mater 40:2248–2255
9. Liu WW, Yan XB, Lang JW, Xue QJ (2012) J Mater Chem 22:8853–8861
10. Li L, Raji Abdul-Rahman O, Fei HL, Yang Y, Samuel Errol LG, Tour James M (2013) ACS Appl Mater Interfaces 5:6622–6627
11. Hsu FH, Wu TM (2014) Synth Metals 198:188–195
12. Hu CC, Chang KH, Lin MC, Wu YT (2006) Nano Lett 6:2690–2695
13. Li ZP, Mi YJ, Liu XH, Liu S, Yang SR, Wang JQ (2011) J Mater Chem 21:14706–14711
14. Tang W, Gao XW, Zhu YS, Yue YB, Shi Y, Wu YP, Zhu K (2012) J Mater Chem 22:20143–20145
15. Liu ZL, Tay SW, Li X (2011) Chem Commun 47:12473–12475
16. Camacho Bragado GA, Jose Yacaman M (2006) Appl Phys A Mater Sci Process 82:19–22
17. Irmawati R, Shafizah M (2009) Inter J Basic Appl Sci 9:34–36
18. Shakir I, Shahid M, Yang HW, Kang DJ (2010) Electrochim Acta 56:376–380
19. Takasu Y, Matsuo C, Ohnuma T, Ueno M, Murakami Y (1999) Electrochem 67:1187–1188
20. Sugimoto W, Ohnuma T, Murakami Y, Takasu Y (2001) Electrochem Solid State Lett 4:A145–A147

21. An KH, Jeon KK, Heo JK, Lim SC, Bae J, Lee YH (2002) J The Electrochem Soc 149:A1058–A1062

22. Fan LZ, Joachim M (2006) Electrochem Commun 8:937–940

23. Xu CH, Sun J, Gao L (2011) J Mater Chem 21:11253–11258

24. Liu Y, Wang HH, Zhou J, Bian LY, Zhu EW, Hai JF, Tang J, Tang WH (2013) Electrochim Acta 112:44–52

25. Wang WJ, Hao QL, Lei W, Xia XF, Wang X (2012) RSC Adv 2:10268–10274

26. Han GQ, Liu Y, Kan EJ, Tang J, Zhang LL, Wang HH, Tang WH (2014) RSC Adv 4:9898–9904

27. Lufrano F, Staiti P, Minutoli M (2004) J The Electrochem Soc 151:A64–A68

28. Weast RC, Astle MJ (1981) CRC handbook of chemistry and physics, 62nd edn. CRC Press Inc., Boca Raton, FL

29. Davies A, Audette P, Farrow B, Hassan F, Chen ZW, Choi JY, Yu AP (2011) J Phys Chem C 115:17612–17620

30. Subba Reddy CV, Walker Edwin Jr H, Wen C, Mho SI (2008) J Power Sources 183:330–333

31. Mendoza-Sanchez B, Brousse T, Ramirez-Castro C, Nicolosi V, Grant PS (2013) Electrochim Acta 91:253–260

32. Liu CG, Yu ZN, Neff D, Zhamu A, Jang Bor Z (2010) Nano Lett 10:4863–4868

33. Liu Y, Zhang BH, Yang YQ, Chang Z, Wen ZB, Wu YP (2013) J Mater Chem A 1:13582–13587

34. Zhang X, Zeng XZ, Yang M, Qi YX (2014) ACS Appl Mater Interfaces 6:1125–1130